

www.acsaem.org Article

Bilayer Luminescent Solar Concentrators with Enhanced Absorption and Efficiency for Agrivoltaic Applications

John Keil,§ Yaling Liu,§ Uwe Kortshagen,* and Vivian E. Ferry*



Cite This: ACS Appl. Energy Mater. 2021, 4, 14102-14110



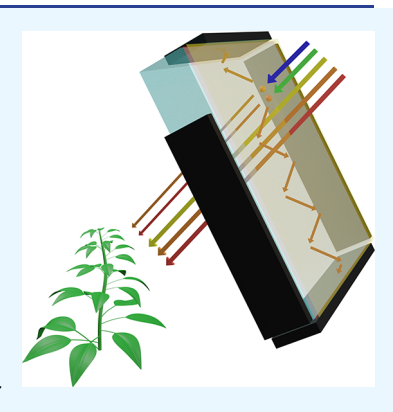
ACCESS

III Metrics & More

Article Recommendations

s) Supporting Information

ABSTRACT: Luminescent solar concentrators are a promising route to environmentally integrated photovoltaics, acting as multifunctional systems that simultaneously generate electricity and transmit sunlight. For agrivoltaic applications, the ability to tune the transmission spectrum of the LSC to optimize crop growth while generating electricity is essential. Here we study a bilayer luminescent solar concentrator composed of a film of Si nanocrystals embedded in poly(methyl methacrylate) and a film of CdSe/CdS nanocrystals embedded in poly(cyclohexylethylene) for potential application in agrivoltaics. Position-dependent photoluminescence measurements demonstrate exceptionally high waveguide efficiency for the Si NC layer, and the films have relatively low diffuse transmission and reflection, indicating low levels of scattering. Using Monte Carlo ray-tracing simulations and experimental characterization, we show that the CdSe/CdS NC layer primarily increases the absorption efficiency of the Si NC-based LSC through a combination of direct absorption enhancement and sensitization. This bilayer system offers significant transmission spectrum tunability across the absorption bands of chlorophyll, which may be useful for agrivoltaic studies of different crop species.



KEYWORDS: luminescent solar concentrator, agrivoltaics, nanocrystals, quantum dots, greenhouse, photoluminescence, nanocomposite, photovoltaics

1. INTRODUCTION

The commercial greenhouse market is expected to expand over the next several years, offering high-yield agriculture and reduced water consumption for expanding populations. However, commercial greenhouses also have significant power needs for precision climate control, lighting, sensing, and other control mechanisms, highlighting the need for onsite power generation under a variety of weather conditions. 1-3 The luminescent solar concentrator (LSC) is an ideal greenhouse window architecture: LSCs are semitransparent, light-harvesting devices designed to spectrally shift and concentrate broadband, diffuse sunlight onto small area photovoltaic (PV) cells to generate electricity while maintaining transmission.4 The LSC itself is a semitransparent waveguide with embedded luminophores; the luminophores absorb solar radiation and reemit light into a spectral range that is more optimal for PV conversion, and the waveguide concentrates that emitted light onto adjacent PV cells. The semitransparent nature of this PV system enables integration in a variety of environments where partial transparency provides either additional functionality or aesthetic benefits. For agrivoltaic applications specifically, the LSC additionally filters light transmission for enhanced crop growth. 5,6

Several studies have demonstrated plant sensitivity to different illumination conditions and have obtained beneficial results from manipulating the relative intensity from different wavelength ranges incident on the crops. 6–10 For example, one

study grew red romaine lettuce under different combinations of LED light sources and found a combination of a RGB (R = 635 nm, G = 520 nm, B = 460 nm) light, and a far red (745 nm) light yielded the best leaf expansion and shoot biomass. Other studies have shown that at higher blue light percentages of the total incident spectrum there is a decrease in growth and dry mass for various plant species. 9,10 Recently, CuInS2/ZnS quantum dot films were used to modify the spectral quality of transmitted light incident on red romaine lettuce, and the plants had increased edible dry and fresh mass.⁶ These studies indicate that electricity generation solutions that decrease the transmission of blue light and increase transmission of red light, as in the LSC which absorbs blue sunlight and shifts emission to longer wavelengths, are particularly promising routes to cogenerating electricity and crop production. However, to deeply understand the effects of the filtered spectrum on the germination and development of different crop species, LSCs with tailored and tunable transmission spectra are needed.

Received: September 14, 2021 Accepted: November 9, 2021 Published: November 22, 2021





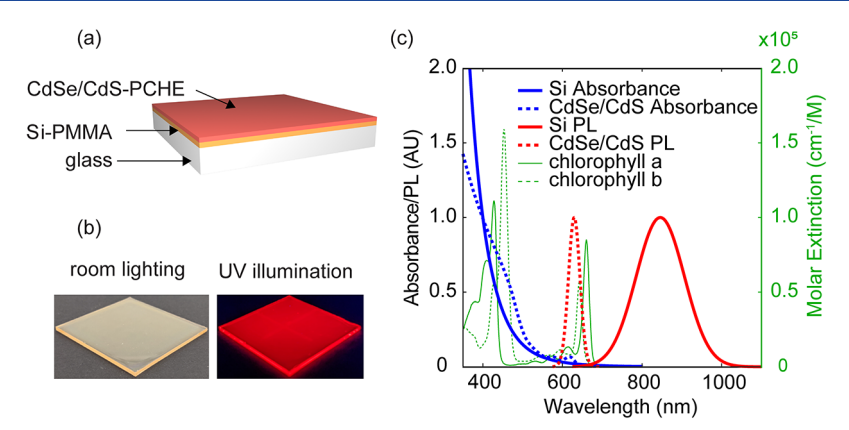


Figure 1. (a) Schematic of the bilayer device along with (b) two photographs of the bilayer device under room light and UV illumination. (c) Normalized absorbance and PL spectra of the Si and CdSe/CdS NCs and the molar extinction coefficient for chlorophyll a and b.

Here, we create bilayer LSCs consisting of two different luminophores to tune the transmission while also improving light collection for electricity generation. The first layer is based on Si nanocrystal (NC) quantum dots, which have received attention recently for use as LSC luminophores due to their desirable optical properties. ^{11–13} Si NCs are indirect band gap semiconductors and exhibit exceptionally low overlap between their absorption and photoluminescence (PL) spectra, which result in remarkably high waveguide efficiencies in LSCs. Si NCs are also nontoxic and composed of earth abundant materials, making them safer and less expensive to synthesize. To achieve high absorption efficiency with an LSC composed of Si NCs, however, the NC-polymer nanocomposite films must be relatively thick and contain a high concentration of NCs. There is an upper limit to the NC concentration before significant nanocrystal agglomeration occurs, which dramatically increases scattering and reduces LSC optical efficiency. 11,12

An alternative strategy is to make a bilayer system of two different luminophores. This second luminophore could either act as the LSC luminophore on its own, broadening the absorption spectrum and emitting over a different spectral range, or, if the second luminophore emits across a spectral range that Si NCs absorb, it can sensitize Si absorption. This type of device is fundamentally different from both tandem LSCs and dual band LSCs, 14-16 as the luminophores are not separated by a low index layer, and the PL from each luminophore is coupled into the same waveguide and directed onto the same PV cell. The low index air gap between waveguides in tandem architectures induces more reflection from the additional air-glass interfaces, which reduces absorption efficiency of the second junction and reduces overall LSC transmission. For the agrivoltaic applications mentioned above, the bilayer system is advantageous as it allows for the concentrations and thicknesses of each luminophore to be tuned individually, enabling greater tunability over the transmission spectrum. By putting the nanocrystals in different polymer layers, the concentration and chemical functionality can be optimized for each luminophore rather than compromising to make a blended system. Furthermore, the bilayer system simplifies the manufacturing and installation process significantly, as a single coating with one PV cell would be less expensive to install onto glass than multiple waveguides each with their own solar cell.

Here we use CdSe/CdS core/shell quantum dots as the second luminophore, since the band gap of these luminophores

can be tuned across the visible spectrum, and these nanocrystals exhibit high PL quantum yields (PLQYs) due to the passivating CdS shell.¹⁷ We have previously shown that CdSe/CdS NCs can be dispersed well into a matrix of poly(cyclohexylethylene) (PCHE), creating high quality nanocomposite thin films for LSCs.¹⁸ This combination of material systems allows for facile fabrication of bilayers, since PCHE and PMMA are dispersed in orthogonal solvents.¹⁸ Our study uses a combination of experimental and computational methods to evaluate the absorption, light propagation, and efficiency of these bilayer devices. We also evaluate how tuning the optical density of each film influences the chlorophyll band transmission for potential use in agrivoltaic applications.

2. RESULTS AND DISCUSSION

The overall structure of the LSC studied here is depicted schematically in Figure 1a and consists of a glass substrate, followed by a Si NC-PMMA film and then by a film of CdSe/ CdS-PCHE deposited on top of the Si-PMMA film. Details of the synthesis of both sets of nanocrystals are provided in the Methods section. To form this structure, we deposited a Si NC-PMMA composite film with ~1.5 Si wt % and a thickness of 83 μ m on a 2 in. \times 2 in. borosilicate glass slide using doctor blade deposition, following a procedure described elsewhere. 12 A film of 7.5 monolayer shell CdSe/CdS NCs dispersed in PCHE was spin-coated directly on the Si-PMMA. To measure the thickness, a separate control film of CdSe/CdS-PCHE was spin-coated on a Si substrate by using the same solution and parameters. The thickness of this control sample was measured at 324 nm by using spectroscopic ellipsometry. Additionally, the thickness of the bilayer reference film of PCHE on PMMA without nanocrystals was measured at 308 nm by using spectroscopic ellipsometry after roughening the backside of the glass substrate. The PLQY of both nanocrystal systems was measured both in solution and embedded in polymer. The assynthesized Si NCs in chloroform had a PLQY of 0.4 and a PLQY of 0.2 when embedded in PMMA in air. According to the previous study,11 the PLQY of Si NCs embedded in PMMA is approximately the same as in chloroform under oxygen-free conditions, while the PLQY of Si NCs decreases when exposed to air. Therefore, the decrease of Si NCs PLQY here can be avoided by fabricating the device in a nitrogenpurged glovebox and deploying an encapsulant to isolate oxygen during use. The PLQY of the CdSe/CdS in octane was 0.73 and 0.58 when embedded in PCHE. An encapsulant could benefit the PLQY CdSe/CdS film as well, but the CdS shell

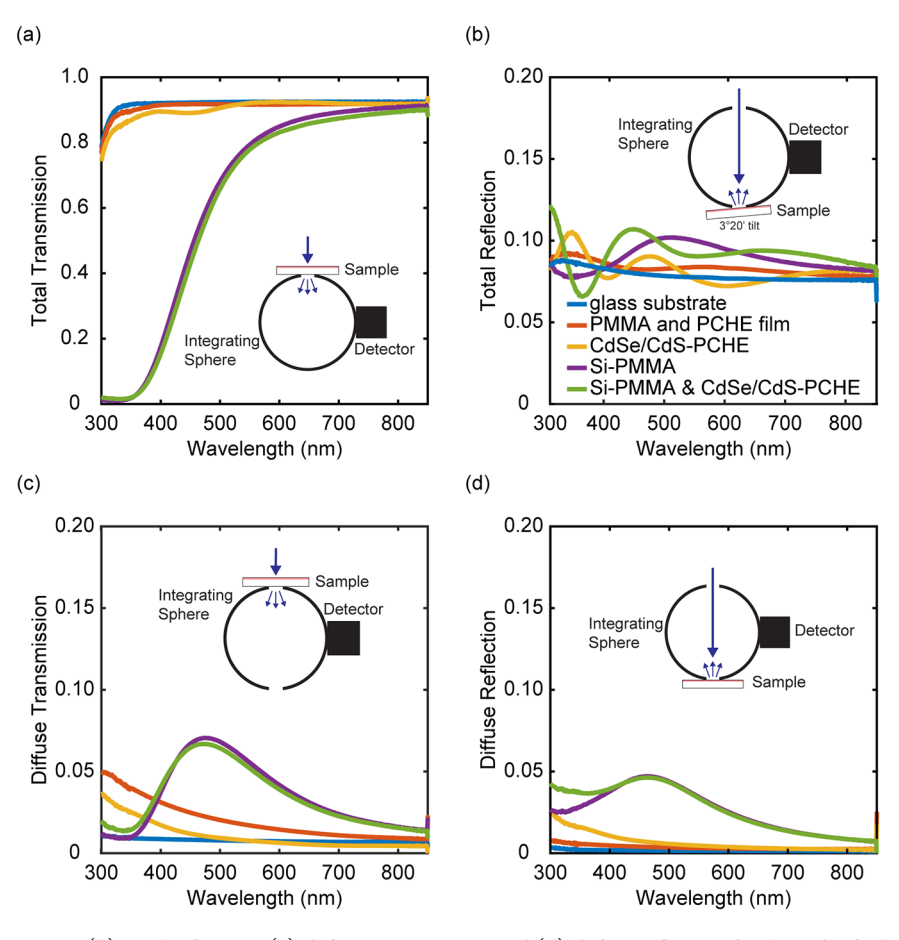


Figure 2. (a) Total transmission, (b) total reflection, (c) diffuse transmission, and (d) diffuse reflection for the CdSe/CdS-PCHE single layer film, Si-PMMA single layer film, and bilayer film. Measurements from an uncoated glass substrate and undoped PMMA and PCHE bilayer films are included for reference.

passivates the surface of the CdSe and prevents significant decrease in the PLQY from exposure to oxygen. The decrease in measured PLQY from embedding the CdSe/CdS in PCHE could be from increased agglomeration and phase separation or from increased CdSe/CdS reabsorption when increasing the concentration compared to the NCs dispersed in octane. ^{19–24}

The photographs in Figure 1b visually indicate the PL from the bilayer device. The absorption and PL spectra of the NCs are shown in Figure 1c along with the molar extinction coefficients of chlorophyll a and b taken from the literature.²⁵ We note that the Soret bands of both chlorophyll a and b overlap significantly with the absorption bands of the nanocrystals, and the Q bands do not. However, the Q bands overlap (by different amounts) with the PL maximum of the CdSe/CdS NCs. Because some of the luminescent light absorbed and emitted by the CdSe/CdS will escape from the concentrator, this outcoupled light could be absorbed by crop species underneath the concentrator. The intensity of PL that would be outcoupled to the plants is lower than the intensity of the PL coupled into waveguide modes, but the additional light across the photosynthetic action spectrum of certain plant species could still promote plant growth, as observed in previous studies.⁶ Tuning the exact size of the CdSe/CdS nanocrystals could allow for greater overlap with the Q bands of either chlorophyll *a* or *b*.

To characterize the spectral and angular properties of the bilayer LSCs, we measured the total and diffuse transmission and reflection (Figure 2). Measurements were also performed

on single layer CdSe/CdS-PCHE and Si-PMMA LSCs, the latter before CdSe/CdS-PCHE deposition, at the same concentrations and thicknesses as the bilayer LSC. Both the single layer CdSe/CdS-PCHE film and the single layer Si-PMMA films showed decreases in total transmission (Figure 2a) compared to their respective undoped references, corresponding to an increase in absorption from the NC incorporation. When the CdSe/CdS-PCHE film was added to the Si-PMMA film to create the bilayer device, the total transmission decreased slightly. The total transmission results confirm that the nanocomposite films are absorbing as expected, with the CdSe/CdS-PCHE layer increasing the absorption slightly compared to the single layer of Si-PMMA. The total reflection (Figure 2b) for all samples containing a PCHE film or a film of CdSe/CdS-PCHE exhibit oscillations due to thin film interference effects. The oscillations from CdSe/CdS-PCHE films have higher amplitudes due to the higher refractive index of the composite, which is consistent with previous results¹⁸ and with the expected reflection from transfer matrix calculations for a PCHE film with and without embedded CdSe/CdS NCs (Figure S6). The increased total reflection seen for the single layer Si-PMMA film is from backscattered light.

The diffuse transmission (Figure 2c) remained relatively low upon addition of the NCs, which indicates minimal scattering in the nanocomposite films. The highest diffuse transmission occurred in the Si-PMMA film and the bilayer system, with a maximum at around 480 nm. The diffuse transmission

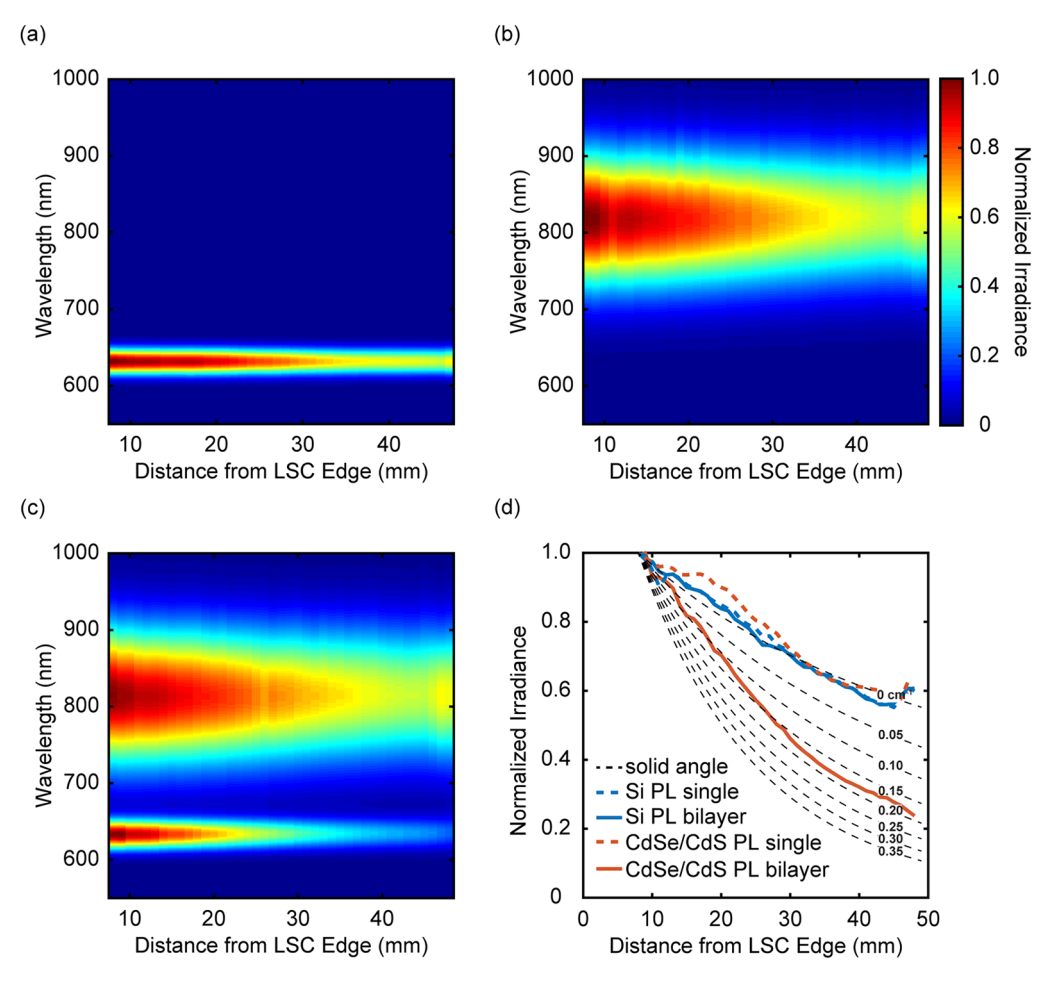


Figure 3. Wavelength and distance resolved normalized irradiance for the (a) CdSe/CdS-PCHE single layer, (b) Si-PMMA single layer, and (c) bilayer film. (d) Peak normalized irradiance for the different devices with analytically derived solid angle estimates for different attenuation coefficients. The normalization was performed with respect to the PL spectrum of each luminophore.

decreases at shorter wavelengths because of the strong increase in absorption, which prevents the transmission of scattered light. A similar trend is observed in the diffuse reflection measurements (Figure 2d). The measured haze for the bilayer film was 5.7%. On the basis of previous results where 83 μ m thick Si-PMMA films had a haze exceeding 40% from nanocrystal agglomeration, we assume that the attenuation of light propagating through these films is dominated by absorption rather than scattering.

To investigate the light propagation and waveguide efficiency of the LSCs, the PL at the edge of the concentrator was measured as a function of the position of the excitation light source. A 405 nm LED light source with a 0.5 mm spot size directed downward on top of the films was scanned across the samples in 1 mm steps, and an integrating sphere was coupled to one side of the waveguide to collect the concentrated PL at each excitation position. The collected intensity spectra for each distance were calibrated to absolute irradiance, and then the PL spectra at each position were fit to a Gaussian distribution. Further details are shown in Figure S7. The spectra with respect to the horizontal distance from the edge of the LSC to the light source are displayed in Figures 3a—c. In Figure 3c, normalization was performed with respect to each NC's own PL spectrum.

The CdSe/CdS nanocrystals emit in the visible, and the Si nanocrystals emit in the near-infrared (NIR), as is clearly seen

in the single layer samples (Figures 3a,b). The normalized irradiance in these single layer samples decreases with increasing excitation distance to ~60% of the peak for both cases. The slight increase in irradiance at the end is real and due to reflection and scattering off the back edge of the LSC. When compared to the bilayer sample (Figure 3c), the Si PL looks nearly identical with the single layer case, but there is a noticeable increase in the CdSe/CdS attenuation in the bilayer sample.

The attenuation observed in these measurements is a combination of waveguide losses and the changing solid angle between the light source and the detector. To unravel these effects, Figure 3d shows the peak normalized irradiance as a function of light source distance from the LSC edge. The reference lines are the different attenuation coefficients, assuming an analytically calculated decrease in irradiance from the changing solid angle. More information about the analytical derivation is provided in Figure S1. By using these reference lines, we can graphically estimate the attenuation coefficient of the PL propagating through the waveguide. The Si NCs in both the single layer and the bilayer systems closely matched the solid angle reference line with an attenuation coefficient of 0 cm⁻¹. This means the Si NC PL coupled into total internal reflection modes did not significantly attenuate from reabsorption or scattering, and the waveguide efficiency is exceptionally high. The PL from the single layer of CdSe/CdS

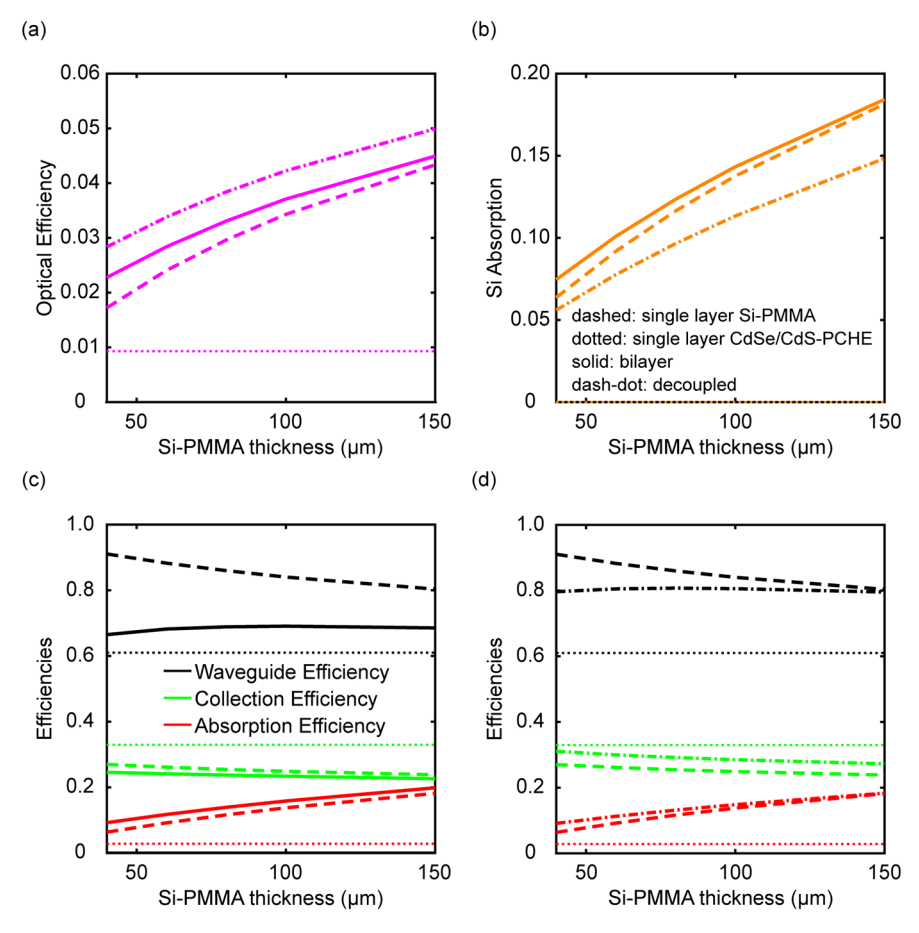


Figure 4. (a) Optical efficiency for a coupled bilayer device and decoupled device composed of Si-PMMA film and a CdSe/CdS-PCHE film while increasing the Si-PMMA thickness. (b) Total Si absorption efficiency while increasing Si-PMMA thickness. Waveguide efficiency, collection efficiency, and absorption efficiency for the (c) coupled bilayer device and the (d) decoupled device. Reference dashed and dotted lines are included for single layer Si-PMMA and CdSe/CdS-PCHE.

also corresponded to a near zero attenuation coefficient. However, the CdSe/CdS PL in the bilayer film showed increased attenuation, with an estimated attenuation coefficient of $\sim 0.17~\rm cm^{-1}$. The increased attenuation was expected and is due to the absorption of the CdSe/CdS NC PL by the Si NCs. Although the Si absorption is lower across the CdSe/CdS PL spectrum than it is at shorter wavelengths, the optical density of the Si-PMMA layer is ~ 0.025 at normal incidence across the CdSe/CdS PL spectrum. The reabsorption of luminescence from the CdSe/CdS NCs by the Si NCs is greater than reabsorption by the CdSe/CdS NCs.

The results were also compared to Monte Carlo ray-tracing simulations for a system of similar LSC size and luminophore optical densities. The attenuation experiment was simulated by using ray-tracing on 2 in. × 2 in. waveguides for a Si-PMMA single layer, CdSe/CdS-PCHE single layer, and a bilayer device. The PLQY of the Si and CdSe/CdS NCs were set at 0.4 and 0.73, respectively, which is close to the experimental PLQY values of the NCs in solution. The resulting attenuation coefficients estimated from the ray-tracing for both single layers and the Si PL in the bilayer device were close to zero (Figure S2). The simulations on the CdSe/CdS PL predicted an increase in attenuation in the bilayer device similar to the experimental results, corresponding to an attenuation coefficient of ~0.19 cm⁻¹. The higher attenuation coefficient is close to the estimated attenuation coefficient from the

experimental results, ~ 0.17 cm⁻¹, and is also due to the absorption of the CdSe/CdS NC PL by the Si NCs.

Given the agreement between experiment and simulation at the smaller scale, we used Monte Carlo simulations to determine whether the addition of the CdSe/CdS layer enhances the performance of the Si-PMMA LSCs for larger area (60 cm × 60 cm) devices (Figure 4). To simulate a strongly absorbing Si-PMMA film with a weaker absorbing CdSe/CdS-PCHE film, the optical density at 350 nm wavelength of incident radiation for the 40 µm Si-PMMA film was set to ~0.5 and scaled proportionately with Si-PMMA thickness. The thickness and optical density at 350 nm for the CdSe/CdS-PCHE film were held constant at 10 μ m and 0.08, respectively. A thickness of 10 μ m was used to stay within the ray optics regime for the ray-tracing simulations. Simulations were also performed for the films on separate, decoupled waveguides with an air gap in between, as this configuration is a common approach for tandem LSCs composed of multiple luminophores. Reference lines are included for single layer Si-PMMA and CdSe/CdS-PCHE efficiencies.

The optical efficiency $(\eta_{\rm opt})$ of both the coupled and decoupled configurations increased when the CdSe/CdS-PCHE layer was added to the system, with the decoupled configuration showing slightly greater enhancement compared to the single layer Si-PMMA LSC (Figure 4a). The optical efficiency is defined as $\eta_{\rm opt} = \Phi_2/\Phi_1$ where Φ_2 is the photon flux concentrated to the sides of the waveguide and Φ_1 is the

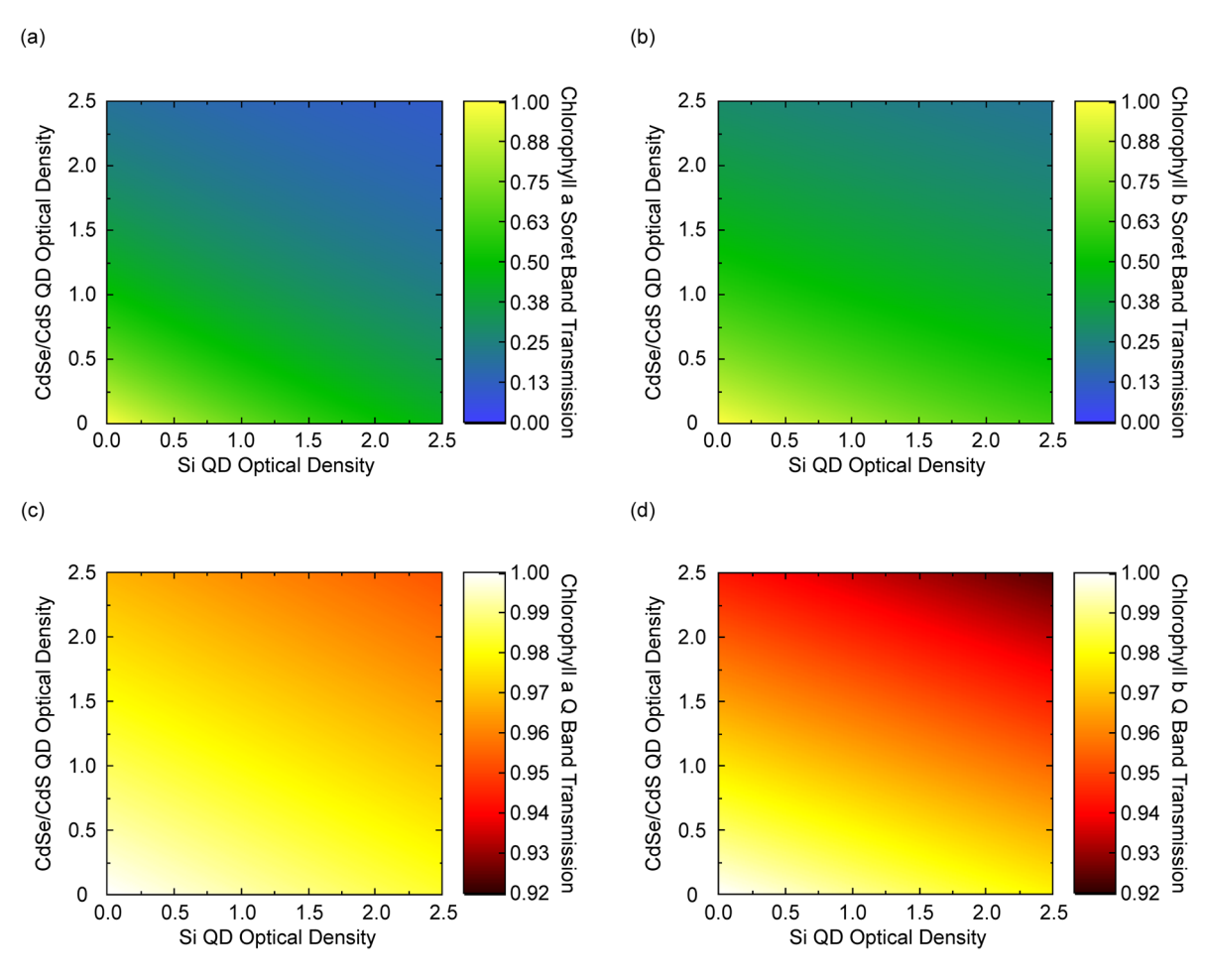


Figure 5. Colormaps of the (a) chlorophyll a Soret band, (b) chlorophyll *b* Soret band, (c) chlorophyll *a* Q-band, and (d) chlorophyll *b* Q-band transmission while adjusting the optical density of the Si and CdSe/CdS NCs. The optical density is defined at 350 nm wavelength of incident radiation.

photon flux incident on the LSC. ²⁶ We can also express the optical efficiency as $\eta_{\rm opt} = \eta_{\rm abs} \eta_{\rm cob}$ where $\eta_{\rm abs}$ is defined as

$$\eta_{\mathrm{abs}} = \frac{\int (1 - T - R) E_{e,\lambda}}{\int E_{e,\lambda}}$$

where T and R are the LSC transmission and reflection, $E_{\rm e,\lambda}$ is the solar spectral irradiance, and $\eta_{\rm col}$ is the fraction of absorbed photons that are successfully concentrated toward the edges of the concentrator. The waveguide efficiency $(\eta_{\rm wg})$, which is the fraction of emitted photons coupled into total internal reflection modes that are concentrated to edges, is directly proportional to the collection efficiency and is also useful for characterizing how efficiently light propagates through the waveguide. More details are provided in the Methods section.

To understand the origin of the enhanced optical efficiency for both device configurations, we calculated the different efficiency terms (Figures 4b–d), as detailed in the Methods section. We first consider the Si absorption, which includes both light that is absorbed by the Si NCs directly and light that was initially absorbed by the CdSe/CdS NCs, emitted, and then absorbed by the Si NCs. Figure 4b shows that the addition of the CdSe/CdS layer increased absorption in the Si in the bilayer configuration, consistent with the experimental measurements that showed that this layer sensitizes the Si absorption. In the decoupled configuration, adding the CdSe/

CdS layer decreases the amount of light absorbed by the Si NCs, since a significant fraction of the incident sunlight is absorbed in the CdSe/CdS layer first. As expected, both devices exhibited an increase in absorption compared to the single junction Si-PMMA LSC because the addition of the CdSe/CdS-PCHE layer added more absorbing material. The absorption efficiency increase for the bilayer device was slightly higher than the decoupled device because of the increased reflection from the additional glass—air interfaces in the latter case.

The waveguide efficiency $\eta_{\rm wg}$ for both systems (Figures 4c,d) decreased with the addition of the CdSe/CdS-PCHE film compared to the single layer Si-PMMA, with a more dramatic decrease for the bilayer LSC. This occurs because the reabsorption losses increase when the two luminophores are coupled together. As the Si-PMMA thickness increased, there was a slight increase in the waveguide efficiency in both cases, since a slightly higher percentage of light is directly absorbed by the Si NCs in thicker films. With such minimal reabsorption for the Si NC PL, this results in an increase in waveguide efficiency. The CdSe/CdS-PCHE single layer film had a lower waveguide efficiency compared to all other LSCs tested due to higher reabsorption losses. The experimentally estimated attenuation coefficient for the single layer CdSe/CdS-PCHE film was near zero (Figure 3), which would correspond to a very high waveguide efficiency. We attribute this inconsistency to the larger LSC size for the ray-tracing simulation. For large area LSCs, the larger overlap between the absorbance and PL spectra for the CdSe/CdS NCs compared to the Si NCs decreases the waveguide efficiency, as the PL coupled into total internal reflection modes has to propagate further to reach the LSC edge. The bilayer device is in a regime, however, where the overall waveguide efficiency is higher compared to the single junction CdSe/CdS-PCHE. This is in part due to the energy transfer from the CdSe/CdS NCs to the Si NCs. Si PL successfully emitted into total internal reflection modes has a very high waveguide efficiency, regardless of whether the absorption was from incident sunlight or from reabsorbed CdSe/CdS PL.

The collection efficiency $\eta_{\rm col}$ shows different trends than $\eta_{\rm wg}$ with the bilayer exhibiting a decreased $\eta_{\rm col}$ and the decoupled device exhibiting an increased $\eta_{\rm col}$ compared to the single layer Si-PMMA. Similar to $\eta_{\rm wg}$, $\eta_{\rm col}$ for the bilayer device decreased because of the increase in reabsorption associated with having the two luminophores in close proximity. For the decoupled device, $\eta_{\rm col}$ was higher when compared to the single layer Si-PMMA because the effective PLQY of the device has a strong effect. The higher PLQY of the CdSe/CdS in these simulations enhanced $\eta_{\rm col}$ despite the increase in reabsorption after the introduction of CdSe/CdS.

Therefore, we see that the addition of the CdSe/CdS layer has different effects for the two geometries. For the decoupled device, the CdSe/CdS-PCHE layer increased both $\eta_{\rm abs}$ and $\eta_{\rm col}$; thus, more sunlight is absorbed, and the absorbed light is utilized more efficiently. Adding the CdSe/CdS-PCHE layer to the bilayer device only increases η_{abs} , but in this case the increase in absorption was more dominant than the decrease in $\eta_{\rm col}$ which led to the overall increase in $\eta_{\rm opt}$. In principle, it would be possible for sensitization in the bilayer case to enhance collection efficiency; if the top layer luminophore had significant reabsorption or a low quantum yield, then transferring these photons to the low reabsorption Si would be beneficial. To test this, Figure S3 compares the waveguide efficiency for the CdSe/CdS layer at different Si PLQYs. We found that the PLQY would have to be close to unity (assuming a CdSe/CdS PLQY of 0.75) for this strategy to provide a collection advantage.

Another advantage of an LSC design with two different luminophores is that the optical density of the luminophores can be adjusted independently to tune the transmission across different spectral regions. This feature may make the bilayer LSC design advantageous for agrivoltaic applications such as greenhouse panels where controlling the spectral quality can influence plant growth and morphology. To demonstrate this tunable transmission for our system, the transmission of the Soret band and the Q-band was calculated for both chlorophyll *a* and chlorophyll *b* while adjusting the optical density of Si and CdSe/CdS NCs. We define the chlorophyll band transmission as

$$T_{\rm Chl} = \frac{\int T_{\rm LSC}(\lambda) \varepsilon_{\rm Chl}(\lambda) \, d\lambda}{\int \varepsilon_{\rm Chl}(\lambda) \, d\lambda}$$

with the Soret band integrated from 350 to 550 nm and the Q-band integrated from 550 to 700 nm, shown in Figure 5. Changing the optical density for both luminophores tunes the Soret and Q-band transmission for both chlorophyll *a* and *b*. The Soret band transmission spans a larger range than the Q-band transmission because the absorbance of the luminophores

increases with decreasing wavelength, which is potentially advantageous for cases where higher blue light percentage decreases plant mass. 9,10

3. CONCLUSION

This study of bilayer LSCs demonstrates that the addition of a CdSe/CdS composite layer to the top of a Si LSC enhances the optical efficiency by increasing the absorption and sensitizing the low-loss Si absorption, while tuning the transmission for modified spectral quality. Concentrated photoluminescence from both luminophores was detected by using attenuation measurements, with increased CdSe/CdS PL attenuation from absorption by the Si NCs. This luminophore interaction decreases the overall collection efficiency of the device but boosts the absorption efficiency, which results in higher optical efficiency. The CdSe/CdS NC to Si NC energy transfer is advantageous as the Si PL has exceptionally high waveguide efficiency with minimal reabsorption. Although the simulations for the decoupled configuration predicted higher optical efficiency than the bilayer, the bilayer device offers numerous advantages, including overall simplicity. This system also allows for control of the transmission across the spectral range of the chlorophyll absorption bands, which makes this type of device promising for agrivoltaic LSC applications.

4. METHODS

Si QD Synthesis and Functionalization. Si QDs were synthesized and functionalized as previously reported.¹¹ Hydrideterminated Si QDs were synthesized in a nonthermal plasma. In the primary plasma region of the reactor, 30 sccm of argon as carrier gas and 14 sccm of 5% silane in 95% helium as precursor gas flowed into the top of the borosilicate glass plasma reactor tube. In the afterglow of the plasma, 100 sccm of hydrogen was injected through an additional inlet for surface passivation purposes. Sixty watts (as indicated by the power supply) of 13.56 MHz radio-frequency (RF) power was applied through an impedance matching network to a pair of concentric ring electrodes fixed on the outside of reactor tube to excite a capacitively coupled plasma. Below the plasma afterglow region, an adjustable orifice was located to control the pressure in the plasma reactor which controls the nanocrystals size and accelerate the nanocrystals for collection by impaction. After that, the synthesized Si QDs were functionalized with methyl 10-undecenoate by hydrosilylation. The hydrosilylation was performed under a nitrogen-purged refluxing condition. Si QDs were dispersed in a 5:1 v/v mixture of mesitylene as a solvent and methyl 10-undecenoate and were heated at 215 °C for 4 h to create an ester-capped particle surface.

Si-PMMA Film Fabrication. The Si-PMMA film fabrication was performed following a similar procedure as previously reported. ¹² A mixture solution of 2.25 mg/mL ester-Si QDs and 0.1 wt % azobis(isobutyronitrile) (AIBN) as thermal initiator in 5 mL of MMA was heated in water bath at 65 °C for about 1 h. The heated solution was then transferred to a 0 °C freezer for at least 1 h to stop the polymerization. After that, the prepolymer solution was brought to room temperature and poured on a clean borosilicate glass substrate behind a doctor blade with a fixed gap of 1270 μ m between the blade and the glass substrate. The blade was swept across the glass substrate so that a thin layer of prepolymer solution over the glass substrate was formed. This thin layer was dried overnight to form the final film. The final film thickness (t) was estimated with

$$t = \frac{1}{2} G f_{\text{solid}}$$

where G is the gap height between the doctor blade and the glass substrate; $f_{\rm solid}$ is the volume fraction of PMMA in the prepolymer solution and was estimated as 13%. ¹²

Photoluminescence Quantum Yield Measurements. Photoluminescence quantum yield measurements were preformed by using

a 2 in. integrating sphere coupled to an OceanOptics USB2000 spectrometer calibrated by using an OceanOptics HL-3 Plus lamp. A 395 nm LED emitted radiation into an integrating sphere where the radiation became isotropic via diffuse reflection at the sphere walls. The emission spectra of QDs were then integrated and divided by the integrated change in excitation signal to calculate the PLQY.

CdSe/CdS-PCHE Film Fabrication. CdSe/CdS NCs were synthesized according to the literature procedures 17,27 and described previously elsewhere. The nanocrystals were imaged by using transmission electron microscopy (Figure S4). The particle size distribution is seen in Figure S5, and the average diameter after shelling is 8.2 nm. The CdSe/CdS-PCHE nanocomposite film fabrication followed previous methods. Briefly, a 200 mg/mL solution of poly(cyclohexylethylene)/octane was created and stirred for 2 h. The polymer solution was filtered through alumina to remove reaction byproducts. 0.6 mL of the PCHE/octane solution, 260 μ L of CdS/CdSe dispersed in octane, and 1.14 mL of octane were mixed.

This solution was spun on 2 in. \times 2 in. borosilicate glass to create the single layer of CdSe/CdS-PCHE and on the Si-PMMA film to create the bilayer device by using a Laurell WS-650Mz-23NPPB spin coater. The solutions were spun with a spin speed of 2000 rpm for 20 s with 500 rpm/s acceleration and then 500 rpm for 40 s with -500 rpm/s acceleration.

UV/Vis Spectrophotometry. Transmission measurements of the polymer—nanocrystal composite films were performed by using a Cary 7000 UV/vis spectrophotometer with a diffuse reflectance accessory. The total transmission measurement was performed by mounting the sample to the integrating sphere transmission port and blocking the back port with a PTFE standard. The PTFE standard was removed for the diffuse transmission measurements. Haze calculations were done according to ASTM D1003-00.²⁹ For the total reflection, the sample is rotated by 3°20′ to couple all reflected light into the integrating sphere, and for diffuse reflection the sample is fixed.

Photoluminescence Attenuation Measurements. The composite films were mounted with the edge coupled to an integrating sphere input port. A 400 nm LED light source with a 0.5 mm spot size was positioned at normal incidence to the film's top surface and scanned across the centerline of the sample directly toward and away from the integrating sphere input port. An Ocean Insight Flame vis—NIR spectrometer was coupled to the integrating sphere to collect the concentrated PL that coupled into the integrating sphere at each excitation position. The spectrometer was calibrated to absolute irradiance by using an Ocean Optics HL-3 plus light source.

Monte Carlo Ray-Tracing Simulations. A Monte Carlo ray-tracing model is used to predict the efficiency of Si and CdSe/CdS NC based LSCs. The simulations inject incident photons at normal incidence on the top surface of the LSC at various wavelengths and tracks the photons as they propagate through and interact with the LSC. The inputs for the model include the optical properties of the CdSe/CdS and Si NCs, the refractive index of the polymers matrices and glass, the thickness of the nanocomposite films, and the optical density of the luminophores. If the photons are moving through either of the nanocomposite films, Beer's law is used to determine the absorption probability at each move step:

$$P_{\rm abs} = 1 - 10^{-OD(\lambda)l_{\rm step}/t_{\rm film}}$$

where $\mathrm{OD}(\lambda)$ is the optical density of the film, l_{step} is the optical path length, and t_{film} is the thickness of the film. All reflection and refraction properties are determined by using Snell's law and Fresnel equations. Photons are considered collected if they are incident on one of the four sides of the waveguide, and the optical efficiency is calculated with

$$\eta_{\text{opt}} = \frac{\int \varphi(\lambda) E_{\text{e},\lambda} \, d\lambda}{\int E_{\text{e},\lambda} \, d\lambda}$$

where $E_{\mathrm{e},\lambda}$ is the solar spectral irradiance and φ is the fraction of photons collected. The collection efficiency η_{col} was calculated

according to $\eta_{\rm col} = \frac{\eta_{\rm opt}}{\eta_{\rm abs}}$. The waveguide efficiency $\eta_{\rm wg}$ was calculated by using $\eta_{\rm wg} = \frac{\eta_{\rm col}}{\eta_{\rm ban}\eta_{\rm pl}}$.

ASSOCIATED CONTENT

5 Supporting Information

The Supporting Information is available free of charge at https://pubs.acs.org/doi/10.1021/acsaem.1c02860.

Solid angle calculations, TEM, and schematic of optical setup (PDF)

AUTHOR INFORMATION

Corresponding Authors

Uwe Kortshagen – Department of Mechanical Engineering, University of Minnesota, Minneapolis, Minnesota 55455, United States; Email: korts001@umn.edu

Vivian E. Ferry — Department of Chemical Engineering and Materials Science, University of Minnesota, Minneapolis, Minnesota 55455, United States; orcid.org/0000-0002-9676-6056; Email: veferry@umn.edu

Authors

John Keil – Department of Chemical Engineering and Materials Science, University of Minnesota, Minneapolis, Minnesota 55455, United States

Yaling Liu – Department of Mechanical Engineering, University of Minnesota, Minneapolis, Minnesota 55455, United States

Complete contact information is available at: https://pubs.acs.org/10.1021/acsaem.1c02860

Author Contributions

§J.K. and Y.L. have equal authorship as first authors.

Notes

The authors declare no competing financial interest.

ACKNOWLEDGMENTS

We are grateful to Marc Hillmyer and Colin Peterson for the PCHE materials. This work was supported partially by the National Science Foundation under Award 1553234 and the MRSEC program under Award DMR-1420013. The authors also acknowledge partial support from the Minnesota Environment and Natural Resources Trust Fund (M.L. 2018, Chp. 214, Art. 4, Sec. 02, Subd. 07a). Part of this work was performed in the College of Science and Engineering Characterization Facility, University of Minnesota, which has received capital funding from the NSF through the MRSEC (Award DMR-2011401) and the NNCI (Award ECCS-2025124) programs.

REFERENCES

- (1) Bersani, C.; Ouammi, A.; Sacile, R.; Zero, E. Model Predictive Control of Smart Greenhouses as the Path towards Near Zero Energy Consumption. *Energies* **2020**, *13* (14), 3647.
- (2) La Notte, L.; Giordano, L.; Calabrò, E.; Bedini, R.; Colla, G.; Puglisi, G.; Reale, A. Hybrid and Organic Photovoltaics for Greenhouse Applications. *Appl. Energy* **2020**, *278*, 115582.
- (3) Barron-Gafford, G. A.; Pavao-Zuckerman, M. A.; Minor, R. L.; Sutter, L. F.; Barnett-Moreno, I.; Blackett, D. T.; Thompson, M.; Dimond, K.; Gerlak, A. K.; Nabhan, G. P.; Macknick, J. E. Agrivoltaics Provide Mutual Benefits across the Food—Energy—Water Nexus in Drylands. *Nat. Sustain.* **2019**, *2* (9), 848—855.

- (4) Yablonovitch, E. Thermodynamics of the Fluorescent Planar Concentrator. *J. Opt. Soc. Am.* **1980**, *70* (11), 1362–1362.
- (5) Corrado, C.; Leow, S. W.; Osborn, M.; Carbone, I.; Hellier, K.; Short, M.; Alers, G.; Carter, S. A. Power Generation Study of Luminescent Solar Concentrator Greenhouse. *J. Renewable Sustainable Energy* **2016**, 8 (4), 043502.
- (6) Parrish, C. H.; Hebert, D.; Jackson, A.; Ramasamy, K.; McDaniel, H.; Giacomelli, G. A.; Bergren, M. R. Optimizing Spectral Quality with Quantum Dots to Enhance Crop Yield in Controlled Environments. *Commun. Biol.* **2021**, *4* (1), 1–9.
- (7) Li, Q.; Kubota, C. Effects of Supplemental Light Quality on Growth and Phytochemicals of Baby Leaf Lettuce. *Environ. Exp. Bot.* **2009**, *67* (1), 59–64.
- (8) Mickens, M. A.; Skoog, E. J.; Reese, L. E.; Barnwell, P. L.; Spencer, L. E.; Massa, G. D.; Wheeler, R. M. A Strategic Approach for Investigating Light Recipes for 'Outredgeous' Red Romaine Lettuce Using White and Monochromatic LEDs. *Life Sci. Space Res.* **2018**, *19*, 53–62.
- (9) Snowden, M. C.; Cope, K. R.; Bugbee, B. Sensitivity of Seven Diverse Species to Blue and Green Light: Interactions with Photon Flux. *PLoS One* **2016**, *11* (10), e0163121.
- (10) Cope, K. R.; Snowden, M. C.; Bugbee, B. Photobiological Interactions of Blue Light and Photosynthetic Photon Flux: Effects of Monochromatic and Broad-Spectrum Light Sources. *Photochem. Photobiol.* **2014**, 90 (3), 574–584.
- (11) Hill, S. K. E.; Connell, R.; Peterson, C.; Hollinger, J.; Hillmyer, M. A.; Kortshagen, U.; Ferry, V. E. Silicon Quantum Dot—Poly(Methyl Methacrylate) Nanocomposites with Reduced Light Scattering for Luminescent Solar Concentrators. *ACS Photonics* **2019**, 6 (1), 170–180.
- (12) Hill, S. K. E.; Connell, R.; Held, J.; Peterson, C.; Francis, L.; Hillmyer, M. A.; Ferry, V. E.; Kortshagen, U. Poly(Methyl Methacrylate) Films with High Concentrations of Silicon Quantum Dots for Visibly Transparent Luminescent Solar Concentrators. *ACS Appl. Mater. Interfaces* **2020**, *12* (4), 4572–4578.
- (13) Sychugov, I. Analytical Description of a Luminescent Solar Concentrator. *Optica* **2019**, *6* (8), 1046–1049.
- (14) Liu, G.; Zhao, H.; Diao, F.; Ling, Z.; Wang, Y. Stable Tandem Luminescent Solar Concentrators Based on CdSe/CdS Quantum Dots and Carbon Dots. *J. Mater. Chem. C* **2018**, *6* (37), 10059–10066
- (15) Wu, K.; Li, H.; Klimov, V. I. Tandem Luminescent Solar Concentrators Based on Engineered Quantum Dots. *Nat. Photonics* **2018**, *12* (2), 105–110.
- (16) Zdrazil, L.; Kalytchuk, S.; Hola, K.; Petr, M.; Zmeskal, O.; Kment, S.; Rogach, A. L.; Zboril, R. A Carbon Dot-Based Tandem Luminescent Solar Concentrator. *Nanoscale* **2020**, *12* (12), 6664–6672.
- (17) Pu, C.; Peng, X. To Battle Surface Traps on CdSe/CdS Core/Shell Nanocrystals: Shell Isolation versus Surface Treatment. *J. Am. Chem. Soc.* **2016**, 138 (26), 8134–8142.
- (18) Connell, R.; Keil, J.; Peterson, C.; Hillmyer, M. A.; Ferry, V. E. CdSe/CdS–Poly(Cyclohexylethylene) Thin Film Luminescent Solar Concentrators. *APL Mater.* **2019**, *7* (10), 101123.
- (19) Yuan, Y.; Krüger, M. Polymer-Nanocrystal Hybrid Materials for Light Conversion Applications. *Polymers* **2012**, *4* (1), 1–19.
- (20) Jin, F.; Zheng, M.-L.; Zhang, M.-L.; Zhao, Z.-S.; Duan, X.-M. A Facile Layer-by-Layer Assembly Method for the Fabrication of Fluorescent Polymer/Quantum Dot Nanocomposite Thin Films. *RSC Adv.* **2014**, *4* (63), 33206–33214.
- (21) Bomm, J.; Büchtemann, A.; Fiore, A.; Manna, L.; Nelson, J. H.; Hill, D.; van Sark, W. G. J. H. M. Fabrication and Spectroscopic Studies on Highly Luminescent CdSe/CdS Nanorod Polymer Composites. *Beilstein J. Nanotechnol.* **2010**, *1* (1), 94–100.
- (22) Meinardi, F.; Colombo, A.; Velizhanin, K. A.; Simonutti, R.; Lorenzon, M.; Beverina, L.; Viswanatha, R.; Klimov, V. I.; Brovelli, S. Large-Area Luminescent Solar Concentrators Based on 'Stokes-Shift-Engineered' Nanocrystals in a Mass-Polymerized PMMA Matrix. *Nat. Photonics* **2014**, *8* (5), 392–399.

- (23) Jeon, H.; Jo, J. H.; Yang, K. P.; Lee, K. Improvement in Efficiency and Stability of Quantum Dot/Polymer Nanocomposite Film for Light-Emitting Diodes Using Refractive Index-Controlled Quantum Dot–Silica Hybrid Particles. *J. Mater. Chem. C* **2019**, 7 (38), 11764–11769.
- (24) Liang, S.; Zhang, M.; Biesold, G. M.; Choi, W.; He, Y.; Li, Z.; Shen, D.; Lin, Z. Recent Advances in Synthesis, Properties, and Applications of Metal Halide Perovskite Nanocrystals/Polymer Nanocomposites. *Adv. Mater.* **2021**, 2005888.
- (25) Du, H.; Fuh, R.-C. A.; Li, J.; Corkan, L. A.; Lindsey, J. S. PhotochemCAD‡: A Computer-Aided Design and Research Tool in Photochemistry. *Photochem. Photobiol.* **1998**, *68* (2), 141–142.
- (26) Klimov, V. I.; Baker, T. A.; Lim, J.; Velizhanin, K. A.; McDaniel, H. Quality Factor of Luminescent Solar Concentrators and Practical Concentration Limits Attainable with Semiconductor Quantum Dots. *ACS Photonics* **2016**, 3 (6), 1138–1148.
- (27) Chen, O.; Chen, X.; Yang, Y.; Lynch, J.; Wu, H.; Zhuang, J.; Cao, Y. C. Synthesis of Metal—Selenide Nanocrystals Using Selenium Dioxide as the Selenium Precursor. *Angew. Chem., Int. Ed.* **2008**, 47 (45), 8638—8641.
- (28) Dement, D. B.; Puri, M.; Ferry, V. E. Determining the Complex Refractive Index of Neat CdSe/CdS Quantum Dot Films. *J. Phys. Chem. C* 2018, 122 (37), 21557–21568.
- (29) ASTM D1003-00, Standard Test Method for Haze and Luminous Transmittance of Transparent Plastics, 2000.